



MOX–Report No. 25/2008

Mathematics in the wind

DAVIDE DETOMI, NICOLA PAROLINI, ALFIO QUARTERONI

MOX, Dipartimento di Matematica “F. Brioschi”
Politecnico di Milano, Via Bonardi 29 - 20133 Milano (Italy)

mox@mate.polimi.it

<http://mox.polimi.it>

Mathematics in the wind

D. Detomi⁽¹⁾, N. Parolini⁽²⁾, A. Quarteroni^(1,2)

October 31, 2008

⁽¹⁾ MOX– Modellistica e Calcolo Scientifico
Dipartimento di Matematica “F. Brioschi”
Politecnico di Milano
via Bonardi 9, 20133 Milano, Italy

⁽²⁾ CMCS - Institut d’Analyse et Calcul Scientifique
Ecole Polytechnique Fédérale de Lausanne
Station 8, CH-1015, Lausanne, Switzerland

Introduction

In any sport or human endeavor, coaches regularly state “play to your strengths.” One might not guess that a land-locked, mountainous country like Switzerland would have strengths that would give them a chance at winning the oldest, most competitive sailing competition in the world, the America’s Cup. But it does!

In 2003, in the Harukai Gulf of New Zealand, a Swiss yacht called Alinghi was the surprise winner of the America’s Cup. And in 2007, in the Mediterranean sea near Valencia, Alinghi confirmed its dominance by defeating the New Zealand Team 5 to 2 in a breathtaking final match race.

Mathematics and computational science were involved in Alinghi’s first successes in 2003, when it won the Louis Vuitton Cup and then the America’s Cup by defeating the defending Black Magic Team of New Zealand. Mathematics helped create the design of the boat which brought the defender Alinghi its second triumph in Valencia in 2007. Mathematical models were used in the design phase and again during the competition.

Of course mathematical models alone are not enough to guarantee success in a race as competitive as the America’s Cup: a great team and much luck are needed. We know that people and explorers have been sailing literally since the stone age. It may seem astonishing that, with all the technological progress that has been achieved, sailing is still such a challenge. Alinghi has shown that part of the progress that will likely be made in the future rests on mathematical models and their numerical solution [3, 11, 12, 13].



Figure 1: The Swiss yacht Alinghi, two-time winner of the America's Cup (2003 and 2007). Photo by Ivo Rovira.

1 Mathematics for sailing

In the past few years, Computational Fluid Dynamics (CFD) has become an essential tool in the design and optimization of racing sailboats and in particular America's Cup yachts. The prevalent role of CFD in the design process is demonstrated by the number of numerical simulations on hull and appendage design as well as on sail optimization, that each America's Cup syndicate carries on during the boat design.

An America's Cup yacht is an extremely complex system that should operate optimally in a wide range of sailing conditions. To achieve an optimal configuration, the design of an America's Cup yacht must account for this complexity and requires to set up suitable (experimental and numerical) models able to describe accurately the system.

America's Cup design teams evaluate whether a design change (and all the other design modifications that this change implies) is globally advantageous, based on a Velocity Prediction Program (VPP), which can be used to estimate the boat speed and attitude for any prescribed wind condition and sailing angle. A prediction of boat speed and attitude can be obtained by modelling the balance between the aerodynamic and hydrodynamic forces acting on the boat. For example, on the water plane, a steady sailing condition is obtained imposing two force balances in x direction (aligned with the boat velocity) and y direction (normal to x on the water plane) and a heeling moment balance around the centerline of the boat:

$$\begin{aligned}
 \mathbf{D}_h + \mathbf{T}_a &= \mathbf{0}, \\
 \mathbf{S}_h + \mathbf{S}_a &= \mathbf{0}, \\
 \mathbf{M}_h + \mathbf{M}_a &= \mathbf{0},
 \end{aligned}
 \tag{1}$$

where \mathbf{D}_h is the hydrodynamic drag (along the course direction), \mathbf{T}_a is the aerodynamic thrust, \mathbf{S}_h is the hydrodynamic side force perpendicular to the course, \mathbf{S}_a is the aerodynamic side force, \mathbf{M}_h and \mathbf{M}_a are, respectively, the hydro mechanical righting moment

and the aerodynamic heeling moment around the boat mean line. The angle β_Y between the course direction and the boat centerline is called *yaw* angle. The aerodynamic thrust and side force can be seen as a decomposition in the reference system aligned with the course direction of the aerodynamic lift and drag which are defined on a reference system aligned with the apparent wind direction. Similar balance equations can be obtained for the other degrees of freedom.

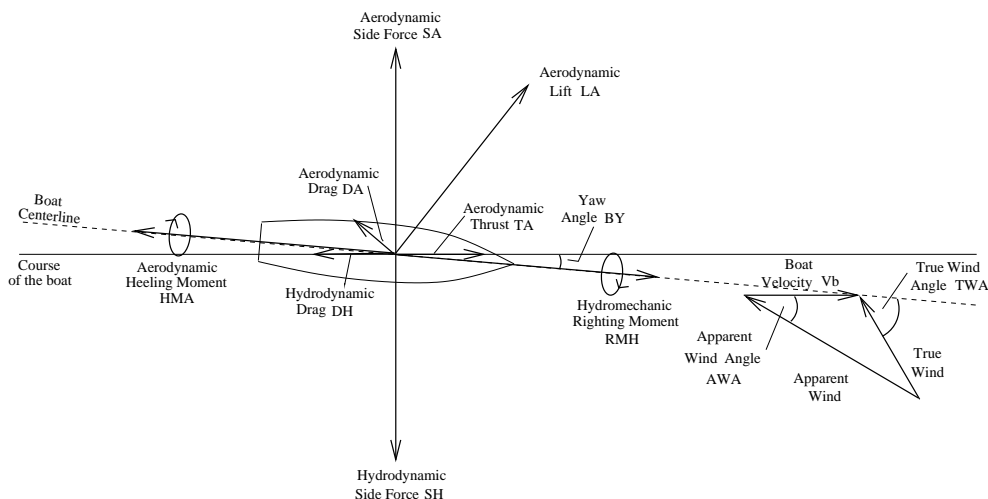


Figure 2: Forces and moments on the water plane.

All the terms in system (1) are modelled in the VPP as functions of boat speed, heel angle and yaw angle. Suitable correlations between the degrees of freedom of the system and the different force components can be obtained based on different sources of data: experimental results, theoretical predictions and numerical simulations.

The role of advanced numerical simulations is to supply accurate estimates of the forces acting on the boat in different sailing conditions in order to improve the reliability of the prediction of the overall performance associated with a given design configuration.

2 Governing equations and numerical approximation

2.1 The flow equations

Let Ω denote the three-dimensional computational domain in which the flow equations will be solved. If $\hat{\Omega}$ is a region surrounding the boat B , the computational domain is the complementary of B w. r. to $\hat{\Omega}$, that is $\Omega = \hat{\Omega} \setminus B$. The equations that govern the flow around B are the density-dependent (or inhomogeneous) incompressible Navier–Stokes equations, which read:

$$\frac{\partial \rho}{\partial t} + \nabla \cdot (\rho \mathbf{u}) = 0, \quad (2)$$

$$\frac{\partial(\rho \mathbf{u})}{\partial t} + \nabla \cdot (\rho \mathbf{u} \otimes \mathbf{u}) - \nabla \cdot \boldsymbol{\tau}(\mathbf{u}, p) = \rho \mathbf{g}, \quad (3)$$

$$\nabla \cdot \mathbf{u} = 0, \quad (4)$$

for $\mathbf{x} \in \Omega$ and $0 < t < T$, and where ρ is the (variable) density, \mathbf{u} is the velocity field, p is the pressure, $\mathbf{g} = (0, 0, g)^T$ is the gravity acceleration, and $\boldsymbol{\tau}(\mathbf{u}, p) = \mu(\nabla \mathbf{u} + \nabla \mathbf{u}^T) - p\mathbf{I}$ is the stress tensor with μ indicating the (variable) viscosity. The above equations have to be complemented with suitable initial conditions and boundary conditions. For the latter we typically consider a given velocity profile at the inflow boundary, with a flat far field free-surface elevation.

In the case we are interested in, the computational domain Ω is made of two regions, the volume Ω_w occupied by the water and that Ω_a occupied by the air. The interface Γ separating Ω_w from Ω_a is the (unknown) free-surface, which may be a disconnected two-dimensional manifold if wave breaking is accounted for. The unknown density ρ actually takes two constant states, ρ_w (in Ω_w) and ρ_a (in Ω_a). The values of ρ_w and ρ_a depend on the fluid temperatures, which are considered to be constant in the present model. The fluid viscosities μ_w (in Ω_w) and μ_a (in Ω_a) are constants which depend on ρ_w and ρ_a , respectively.

The set of equations (2)-(4) can therefore be regarded as a model for the evolution of a two-phase flow consisting of two immiscible incompressible fluids with constant densities ρ_w and ρ_a and different viscosity coefficients μ_w and μ_a . In this respect, in view of the numerical simulation, equation (2) represents a candidate for updating the (unknown) interface location Γ , then equations (3)-(4) will provide a coupled system of Navier–Stokes equations in the two sub-domains Ω_w and Ω_a :

$$\frac{\partial(\rho_w \mathbf{u}_w)}{\partial t} + \nabla \cdot (\rho_w \mathbf{u}_w \otimes \mathbf{u}_w) - \nabla \cdot \boldsymbol{\tau}_w(\mathbf{u}_w, p_w) = \rho_w \mathbf{g},$$

$$\nabla \cdot \mathbf{u}_w = 0,$$

in $\Omega_w \times (0, T)$,

$$\frac{\partial(\rho_a \mathbf{u}_a)}{\partial t} + \nabla \cdot (\rho_a \mathbf{u}_a \otimes \mathbf{u}_a) - \nabla \cdot \boldsymbol{\tau}_a(\mathbf{u}_a, p_a) = \rho_a \mathbf{g},$$

$$\nabla \cdot \mathbf{u}_a = 0,$$

in $\Omega_a \times (0, T)$. We have set $\boldsymbol{\tau}_w(\mathbf{u}_w, p_w) = \mu_w(\nabla \mathbf{u}_w + \nabla \mathbf{u}_w^T) - p_w \mathbf{I}$, while $\boldsymbol{\tau}_a(\mathbf{u}_a, p_a)$ is defined similarly.

The free surface Γ is a sharp interface between Ω_w and Ω_a , on which the normal components of the two velocities $\mathbf{u}_a \cdot \mathbf{n}$ and $\mathbf{u}_w \cdot \mathbf{n}$ should agree. Furthermore, the

tangential components must match as well since the two flows are incompressible. Thus we have the following kinematic condition

$$\mathbf{u}_a = \mathbf{u}_w \quad \text{on } \Gamma. \quad (5)$$

Moreover, the forces acting on the fluid at the free-surface are in equilibrium. This is a dynamic condition expressing the property that the normal forces on either side of Γ are of equal magnitude and opposed direction, while the tangential forces must agree in both magnitude and direction:

$$\boldsymbol{\tau}_a(\mathbf{u}_a, p_a) \cdot \mathbf{n} = \boldsymbol{\tau}_w(\mathbf{u}_w, p_w) \cdot \mathbf{n} + \kappa \sigma \mathbf{n} \quad \text{on } \Gamma, \quad (6)$$

where σ is the surface tension coefficient, that is a force per unit length of a free surface element acting tangential to the free-surface. Having surface tension is a property of the liquid and depends on the temperature as well as on other factors. The quantity κ in (6) is the curvature of the free-surface, $\kappa = R_{t_1}^{-1} + R_{t_2}^{-1}$, where R_{t_1} and R_{t_2} are radii of curvature along the coordinates (t_1, t_2) of the plane tangentially to the free-surface (orthogonal to \mathbf{n}).

The free-surface interface between air and water is tracked using the Volume of Fluid (VOF) method [4]. The RANS equations, as well as all the partial differential equations required in the turbulence, transition (see Section 2.2) and free-surface models, are solved using a vertex-based finite volume method [15].

2.2 Turbulence and transition models

The flow around an IACC boat in standard race regime exhibits turbulent behavior over the vast majority of the yacht surface. Turbulent flows are characterized by being highly unsteady, three-dimensional, containing vortices and coherent structures which stretch and increase the intensity of turbulence. Even more importantly, they fluctuate on a broad range of scales (in space and time). This feature makes the so-called direct numerical simulation (DNS) unaffordable. The adoption of a RANS (Reynolds Averaged Navier-Stokes) model is then required to deal with the turbulent nature of the flow.

The SST (Shear Stress Transport) model proposed by Menter [9] is an eddy-viscosity model defined as a combination of a $k - \omega$ model (in the inner boundary layer) and $k - \varepsilon$ model (in the outer region of and outside of the boundary layer). A blending function ensures a smooth transition between the two models. The $k - \varepsilon$ model has two main weaknesses: it over-predicts the shear stress in adverse pressure gradient flows because of too large length scale (due to low dissipation) and it requires near-wall modification (i.e. low-Reynolds number damping terms). The $k - \omega$ model is better at predicting adverse pressure gradient flow and the standard model of Wilcox [18] does not use any damping functions. However, the disadvantage of the standard $k - \omega$ model is that it depends on the free-stream value of ω [8]. In order to improve both the $k - \varepsilon$ and the $k - \omega$ model, Menter [9] combines the two models. Prior to that, it is convenient to transform the $k - \varepsilon$ model into a $k - \omega$ model using the relation $\omega = \varepsilon / (c_\mu k)$.

The two partial differential equations governing the turbulent kinetic energy k and the turbulent frequency ω then reads:

$$\begin{aligned}\frac{D(\rho k)}{Dt} &= P_k - D_k + \nabla \cdot ((\mu + \sigma_k \mu_t) \nabla k), \\ \frac{D(\rho \omega)}{Dt} &= \alpha \rho \frac{P_k}{\mu_t} - D_\omega + Cd_\omega + \nabla \cdot ((\mu + \sigma_k \mu_t) \nabla \omega),\end{aligned}\tag{7}$$

where P_k and P_Ω are production terms, D_k and D_ω destruction ones and Cd_ω results from transforming the ε equation into an equation for ω . The coefficients in the SST model are obtained by combining the value of the coefficients of the standard $k - \omega$ (in the near wall region) to those of the $k - \varepsilon$ model by using a blending function F_1 . We refer to [9] for a detailed description of the model and its parameters.

Eddy-viscosity turbulence models, such as the one described here, are nowadays widely adopted for the simulation of turbulent flows in engineering applications. Indeed, they are able to recover with an acceptable accuracy the global behavior related to the turbulence nature of a flow. In particular, in presence of walls, they supply an accurate description of turbulent boundary layers.

The laminar-turbulent transition is a physical phenomenon as complex as turbulence itself. It involves the nonlinear interaction of flow perturbations that is eventually responsible for the evolution towards a fully turbulent behavior. Many models for transition prediction have been proposed in the past decades [17, 6, 16, 7]. However, only recently transition models have been fully integrated into RANS solver. Among them, the Langtry-Menter transition model [10] is based on a transport equation for the turbulence intermittency γ which can be used to trigger transition locally. The intermittency function is coupled with the SST turbulence model introduced above by turning on the production term of the turbulent kinetic energy downstream of the transition point. In addition to the transport equation for the intermittency, a second transport equation is solved in terms of the transition onset momentum-thickness Reynolds number $\widetilde{\text{Re}}_{\theta t}$. This is done in order to capture the non-local influence of the turbulence intensity, which changes due to the decay of the turbulence kinetic energy in the freestream, as well as due to changes in the free-stream velocity outside the boundary layer. This additional transport equation is an essential part of the model as it relates the empirical correlation to the onset criteria in the intermittency equation and allows the model to be used in general geometries without interaction from the user.

2.3 Boat dynamics as a 6-DOF, buoyant rigid body

The attitude of a boat advancing in calm water or wavy sea is strictly correlated with its performances. For this reason, a state-of-the-art numerical tool for yacht design predictions should be able to account for the boat motion. This requires the coupling between the fluid model and another one able to compute the structure dynamics. In the case at hand, the structural deformations can be neglected and only the rigid body motion of the boat using six degrees of freedom is considered.

Following the approach adopted in [1, 2], two orthogonal Cartesian reference systems are considered: an inertial reference system (O, X, Y, Z) which moves forward with the mean boat speed and a body-fixed reference system (G, x, y, z) , whose origin is the boat center of mass G , which translates and rotates with the boat. The XY plane in the inertial reference system is parallel to the undisturbed water surface and the Z - *axis* points upward. The body-fixed x -axis is directed from bow to stern, y is positive starboard and z upwards.

The dynamics of the boat in the 6 degrees of freedom is determined by integrating the equations of variation of linear and angular momentum in the inertial reference system, as follows

$$m\ddot{\mathbf{X}}_G = \mathbf{F}, \quad (8)$$

$$\bar{\mathbf{T}}\bar{\mathbf{I}}\bar{\mathbf{T}}^{-1}\dot{\bar{\boldsymbol{\Omega}}} + \bar{\boldsymbol{\Omega}} \times \bar{\mathbf{T}}\bar{\mathbf{I}}\bar{\mathbf{T}}^{-1}\bar{\boldsymbol{\Omega}} = \mathbf{M}_G, \quad (9)$$

where m is the boat mass, $\ddot{\mathbf{X}}_G$ is the linear acceleration of the center of mass, \mathbf{F} is the force acting on the boat, $\dot{\bar{\boldsymbol{\Omega}}}$ and $\bar{\boldsymbol{\Omega}}$ are the angular acceleration and velocity, respectively, \mathbf{M}_G is the moment with respect to G acting on the boat, $\bar{\mathbf{I}}$ is the tensor of inertia of the boat about the body-fixed reference system axes and $\bar{\mathbf{T}}$ is the transformation matrix between the body-fixed and the inertial reference system (see [1] for details).

The forces and moments acting on the boat are given by

$$\begin{aligned} \mathbf{F} &= \mathbf{F}_{\text{Flow}} + m\mathbf{g} + \mathbf{F}_{\text{Ext}}, \\ \mathbf{M}_G &= \mathbf{M}_{\text{Flow}} + (\mathbf{X}_{\text{Ext}} - \mathbf{X}_G) \times \mathbf{F}_{\text{Ext}}, \end{aligned}$$

where \mathbf{F}_{Flow} and \mathbf{M}_{Flow} are the force and moment, respectively, due to the interaction with the flow and \mathbf{F}_{Ext} is an external forcing term (which may model, e.g., the wind force on sails) while \mathbf{X}_{Ext} is its application point.

To integrate in time the equations of motion, the second order ordinary differential equations (8-9) are formulated as systems of first order ODE. If we consider, for example, the linear momentum equation (8), it can be rewritten as

$$m\dot{\mathbf{Y}}_G = \mathbf{F}, \quad (10)$$

$$\dot{\mathbf{X}}_G = \mathbf{Y}_G, \quad (11)$$

where \mathbf{Y}_G denotes the linear velocity of the center of mass. This system is solved using an explicit 2-step Adams-Bashforth scheme for the velocity

$$\mathbf{Y}^{n+1} = \mathbf{Y}^n + \frac{\Delta t}{2m}(3\mathbf{F}^n - \mathbf{F}^{n-1}),$$

and a Crank-Nicholson scheme for the position of the center of mass

$$\mathbf{X}^{n+1} = \mathbf{X}^n + \frac{\Delta t}{2}(\mathbf{Y}^{n+1} + \mathbf{Y}^n).$$

For a convergence analysis of the scheme (as well as for a detailed description of the integration scheme for the angular momentum equation), we refer to [5], where it is

shown that second-order accuracy in time is obtained. Moreover, the scheme features adequate stability properties. Indeed, the stability restriction on time step is less severe than the time step required to capture the physical time evolution.

In the coupling with the flow solver, the 6-DOF dynamical system receives at each time step the value of the forces and moments acting on the boat and returns values of new position as well as linear and angular velocity. In the flow solver, these data are used to update the computational grid (by a mesh motion strategy based on elastic analogy) and the flow equations are solved on the new domain through an Arbitrary Lagrangian Eulerian (ALE) approach.

3 A model for the wind-sails fluid-structure interaction

3.1 Mathematical formulation

The sail deformation is due to the fluid motion: the aerodynamic pressure field deforms the sail surfaces and this, in its turn, modifies the flow field around the sails. From a mathematical viewpoint, this yields a coupled system that comprises the incompressible Navier-Stokes equations with constant density $\rho = \rho_{air}$ (3-4) and a second order elastodynamic equation which models the sail deformation as that of a membrane. More specifically, the evolution of the considered elastic structure is governed by the classical conservation laws for continuum mechanics.

Considering a Lagrangian framework, if $\hat{\Omega}_s$ is the reference 2D domain occupied by the sails, the governing equation can be written as follows:

$$\rho_s \frac{\partial^2 \mathbf{d}}{\partial t^2} = \nabla \cdot \boldsymbol{\sigma}_s(\mathbf{d}) + \mathbf{f}_s \quad \text{in } \hat{\Omega}_s \times (0, T], \quad (12)$$

where ρ_s is the material density, the displacement \mathbf{d} is a function of the space coordinates $\mathbf{x} \in \hat{\Omega}_s$ and of the time $t \in [0; T]$, $\boldsymbol{\sigma}_s$ are the internal stresses while \mathbf{f}_s are the external loads acting on the sails (these are indeed the normal stresses $\boldsymbol{\tau}(\mathbf{u}, p) \cdot \mathbf{n}$ on the sail surface exerted by the flowfield). In fact, $\hat{\Omega}_s$ represents a wider (bounded and disconnected) domain which includes also the mast and the yarns as parts of the structural model. The boundary of $\hat{\Omega}_s$ is denoted by $\partial\hat{\Omega}_s$ and $[0; T] \subset \mathbb{R}^+$ is the time interval of our analysis. For suitable initial and boundary conditions and assigned an appropriate constitutive equation for the considered materials (defining $\boldsymbol{\sigma}_s(\mathbf{d})$), the displacement field \mathbf{d} is computed by solving (12) in its weak form:

$$\int_{\hat{\Omega}_s} \rho_s \frac{\partial^2 d_i}{\partial t^2} (\delta d_i) d\mathbf{x} + \int_{\hat{\Omega}_s} \sigma^H_{ik} (\delta \epsilon_{ki}) d\mathbf{x} = \int_{\hat{\Omega}_s} f_{s i} (\delta d_i) d\mathbf{x}, \quad (13)$$

where $\boldsymbol{\sigma}^H$ is the second Piola-Kirchhoff stress tensor, $\boldsymbol{\epsilon}$ is the Green-Lagrange strain tensor and $\delta \mathbf{d}$ are the test functions expressing the virtual deformation. The second coupling condition enforces the continuity of the two velocity fields, \mathbf{u} and $\frac{\partial \mathbf{d}}{\partial t}$, on the sail surface.

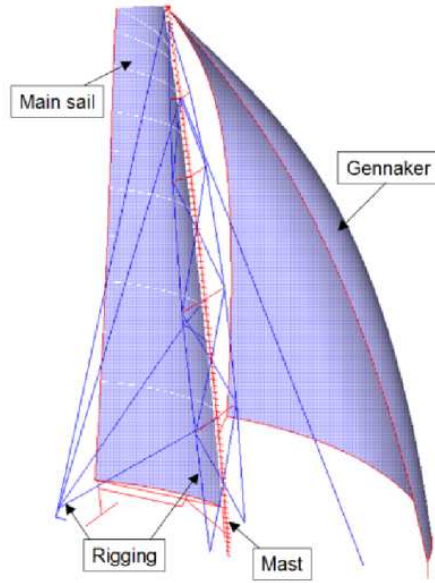


Figure 3: Components considered in the structural model.

3.2 Constitutive equations

The structural model can be partitioned into three different elements: the sails, the yarns and the mast (see Fig. 3). Each of these parts has different materials, different stress conditions and, then, different constitutive equations.

The sails are modelled as thin elastic isotropic membranes, with large displacement and small strains. This model implies a linear description for the material, but also includes a non-linear term due to the geometry in the strain expression. The expression of the Green-Lagrange strain tensor is non-linear in terms of the displacements, but there is a linear relation between the strain tensor ϵ and the second Piola-Kirchhoff tensor σ^H . The mast is thought as an elastic beam under large displacements and small strains. Once again the Green-Lagrange tensor is non-linear, while there is a linear relation between the stress and the strain tensors. Finally the rigging is modelled as elastic cables under large displacements and large strains. Both the Green-Lagrange strain tensor and the stress-strain relation are therefore non-linear. Once the materials properties are known both the stress and strain tensors can be written as non-linear functions of the displacement \mathbf{d} , respectively $\sigma^H(\mathbf{d})$ and $\epsilon(\mathbf{d})$. These expressions close the problem (13), thus allowing the determination of the displacements field \mathbf{d} .

As previously noticed, large displacements are allowed for all the components of the structural model. In this view it is convenient to formulate the problem in a Lagrangian framework always referred to the last deformed configuration and not to the original (design) one.

3.3 Wrinkle model

A particular problem arises when dealing with sails: the latter are described as membranes with zero flexural stiffness and, thus, the idealized membrane cannot sustain any compressive stress. When compressive stresses are about to appear in the membrane, they are immediately released by out-of-plane deformations, i. e. the membrane wrinkles. This phenomenon has to be included in the model. The stress field after wrinkling is modelled as a uniaxial tension field, in which one principal stress is tensile and the other one is zero, moreover the wrinkle direction is assumed to be identical to that of tension lines. In addition, the out-of-plane deformation caused by wrinkling is replaced by the in-plane contraction, whose direction is perpendicular to that of wrinkle. Such in-plane contraction is the zero-energy deformation because its direction coincides with the principal axis corresponding to zero stress. In this context the wrinkled membrane can be treated as a planar problem, and local buckling caused by wrinkling is simplified to the in-plane contraction. For a thorough analysis about the wrinkle model used the reader can refer to [14].

3.4 Numerical solution

Problem (13) has been solved numerically by a traditional finite element formulation, even if the different nature of sails, mast and yarns requires the implementation of specific techniques. The sails have been discretized using triangular three-points elements with linear displacements and constant stresses and strains and the integration on the elements has been performed using a one point Gaussian quadrature scheme. The yarns have been discretized using one-dimensional two points linear elements while the mast has been modelled by using one-dimensional cubic Hermite elements. The resulting formulation of problem (13), after the introduction of the finite elements discretization, reads

$$M\ddot{\mathbf{v}}(t) + \mathbf{K}(\mathbf{v}(t)) = \mathbf{F}(t) \quad (14)$$

where \mathbf{v} are the finite elements nodal variables, M is the mass matrix, $\mathbf{K}(\mathbf{v}(t))$ contains the non-linear elastic nodal forces and \mathbf{F} are the nodal external loads. In the model adopted the damping forces are assumed to be null.

3.5 Fluid-structure coupling algorithm

As previously introduced, the coupling procedure iteratively loops between the fluid solver (passing sail velocities and getting pressure fields) and the structural solver (passing pressures and getting velocities and structural deformations) until the structure undergoes no more deformations because a perfect balance of forces and moments is reached. When dealing with transient simulations, this must be true for each time step and the sail geometry evolves over time as a sequence of converged states. On the other hand, a steady simulation can be thought as a transient one with an infinite time step, such that “steady” means a sort of average of the true (unsteady) solution over time. More formally, we can define two operators called `Fluid` and `Struct` which represent

the fluid and structural solvers, respectively. In particular, **Fluid** can be any procedure which can solve the incompressible Navier-Stokes equations while **Struct** should solve a membrane-like problem, possibly embedding suitable non-linear models to take into account complex phenomena as, for example, the structural reactions due to a fabric wrinkle.

The fixed-point formulation can be reformulated with the new operators as follows:

$$\mathbf{Fluid}(\mathbf{Struct}(p)) = p \quad (15)$$

In this formulation we can clearly recognize the structure of a fixed-point problem. A resolving algorithm can be devised as follows. At a given iteration the pressure field on sails p is passed to the structural solver (**Struct**) which returns the new sail geometries and the new sail velocity fields. Afterwards, these quantities are passed to the fluid solver (**Fluid**) which returns the same pressure field p on sails. Clearly, the “equal” sign holds only at convergence. The resulting fixed-point iteration can be rewritten more explicitly as follows:

Given a pressure field on sails p_k , do:

$$\begin{aligned} (G_{k+1}, \mathbf{U}_{k+1}) &= \mathbf{Struct}(p_k) \\ \bar{p}_{k+1} &= \mathbf{Fluid}(G_{k+1}, \mathbf{U}_{k+1}) \\ p_{k+1} &= (1 - \theta_k)p_k + \theta_k\bar{p}_{k+1} \end{aligned} \quad (16)$$

where G_{k+1} and \mathbf{U}_{k+1} are the sail geometry and the sail velocity field at step $k + 1$, respectively, while θ_k is a suitable acceleration parameter.

Even though the final goal is to run an unsteady simulation, the fluid-structure procedure has to run some preliminary steady couplings to provide a suitable initial condition. The steady run iterates until a converged sail shape and flow field are obtained, where converged means that it does exist a value of k_c such that (15) is satisfied $\forall k > k_c$ (within given tolerances on forces and/or displacements). When running steady simulations the velocity of the sails is imposed to be null at each coupling, thus somehow enforcing the convergence condition (which prescribes null velocities at convergence). This explains why convergence is slightly faster when running steady simulations with respect to transient ones (clearly only when such a solution reflects a steady state physical solution).

4 Computational complexity

The numerical simulations finalized to the optimization of the yacht appendages require the adoption of the finest turbulence and transition models, in order to correctly capture the trade-off between viscous and pressure drag. In particular, the transition model has been found to be essential to recover accurately the viscous drag which is highly influenced by the laminar-turbulent transition location.

However, these models demands extremely fine grids, in particular in the near-wall region and, therefore, the simulations for the appendages entail very large size computational grids (up to 30 millions elements). Since for each grid element we have 8 variables

(3 velocity components, pressure, plus turbulent kinetic energy k , turbulent frequency ω , intermittency γ and transition onset momentum-thickness Reynolds number $\widetilde{Re}_{\theta t}$), the resulting algebraic system involves up to 240 million unknowns.

These simulations were run on the EPFL's Mizar cluster (450 AMD Opteron processors connected by a Myrinet network). A typical run required 30 hours to reach convergence using 32 processors.

The hull dynamics simulations described in Section 2.3 usually require smaller grids with up to 4 million elements. However, in this case one more equation is solved for the volume fraction variable which describes the free-surface evolution and a mesh motion problem has to be solved at each iteration in order to adapt the grid to the boat dynamics. Moreover, when the free-surface computation is included in the model, the simulation requires more iterations to converge. All these factors leads to a CPU time requirements which are typically about 25 hours running on 32 processors.

Concerning the fluid-structural interaction analysis on downwind sails, the first simulations have been run with grids of about 3 millions of elements, with finer meshes over the gennaker/spinnaker surfaces than over the main sail. This different discretization was based on the assumption that the main sail is typically much stiffer and stable than gennaker/spinnaker, thus it seemed more important to refine the mesh and increase the accuracy around the lighter (more deformable) sails. However, further experiments have shown that asymptotic solutions require much finer meshes, at least around 10 millions of elements, and that high accuracy within the channel between the two sails is extremely important to ensure reliable results. This suggested to set the same refinement over the two sails, and the current standard is an element size of few centimeters over the sail edges (where separations may occur) up to 10-20 centimeters over the sail surfaces (which total area is more than 700 m²). Fluid-structure analyses on sails add important complexities to the simulations on hull and appendages, because of the coupling with a deformable structure (while the rest of the boat can reasonably be thought as rigid). When dealing with steady simulations (where null sail velocities are imposed), 5-6 couplings are usually enough to get force variations below few Newton and deformations below 1%. However, when the flow is particularly unstable, the steady approach is clearly not optimal and the simulation does not reach any kind of converged state. In such cases it is better to switch to a transient scheme, where sails have their own velocities and the true sail dynamics can be modelled and evaluated. Transient runs usually show evolving sails, which change their shape (more or less periodically) over time. In this case, at least 60 seconds of real time must be considered in order to have a correct idea about the behavior of the sails under the specified wind conditions. Choosing a time step which reasonably cannot be larger than 0.5 seconds, at least 120 time steps have to be solved with (at least) 3 sub-coupling per time step. In total, this means about 350-400 fluid-structural couplings, which is an extremely time consuming computation if the fluid mesh is large and/or the number of available processors is small.

5 Numerical Results

5.1 Appendages optimization

One of the design areas where CFD simulations play a crucial role is the optimization of the appendages (keel, bulb, winglets and rudder) which should be shaped and sized (within the degrees of freedom left by the strict IACC rules) in order to guarantee global optimal performances.

Full-scale tests are still an invaluable ingredient of the design process: the final step for taking every important design choice is always testing full scale on the real boat. Several days of testing, with the two boats differing by the design detail under investigation, are planned during every America's Cup campaign by all the syndicates.

Nevertheless, intensive numerical simulations are carried on in order to analyze many hundreds of different appendage shape candidates [12, 13].

The design analyses that can be carried out by CFD simulations cover all the possible design variables that define a set of appendages. The great advantage of the numerical approach relies on the possibility to test several different configurations and to have a complete picture of the flow behaviour at every time instant (see Figure 4).

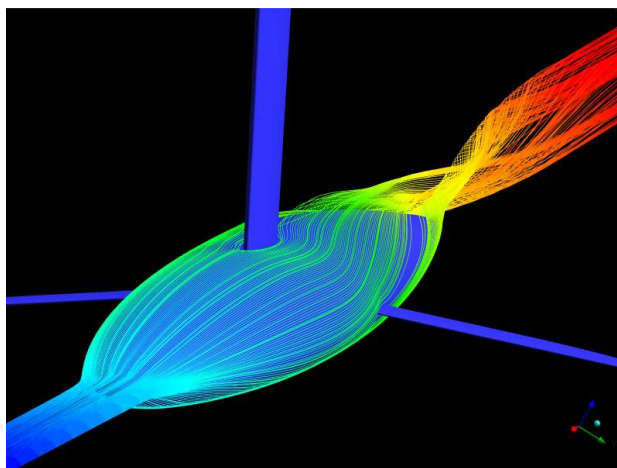


Figure 4: Streamlines around the appendages.

Information about local distribution of flow quantities (such as, e.g. pressure, vorticity and turbulence intensity) can be very useful to improve the hydrodynamic performances. These information can be hardly obtained during a full-scale test and even in a fully equipped experimental facility (wind tunnel or towing tank) each of these data requires the setup of suitable measurement equipments. On the other hand, numerical simulations supply as outcome a complete database of relevant quantities about the considered flow problem.

The fluid-dynamic mechanism underlying the benefits observed when winglets are adopted can be highlighted comparing appendage configurations with and without winglets,

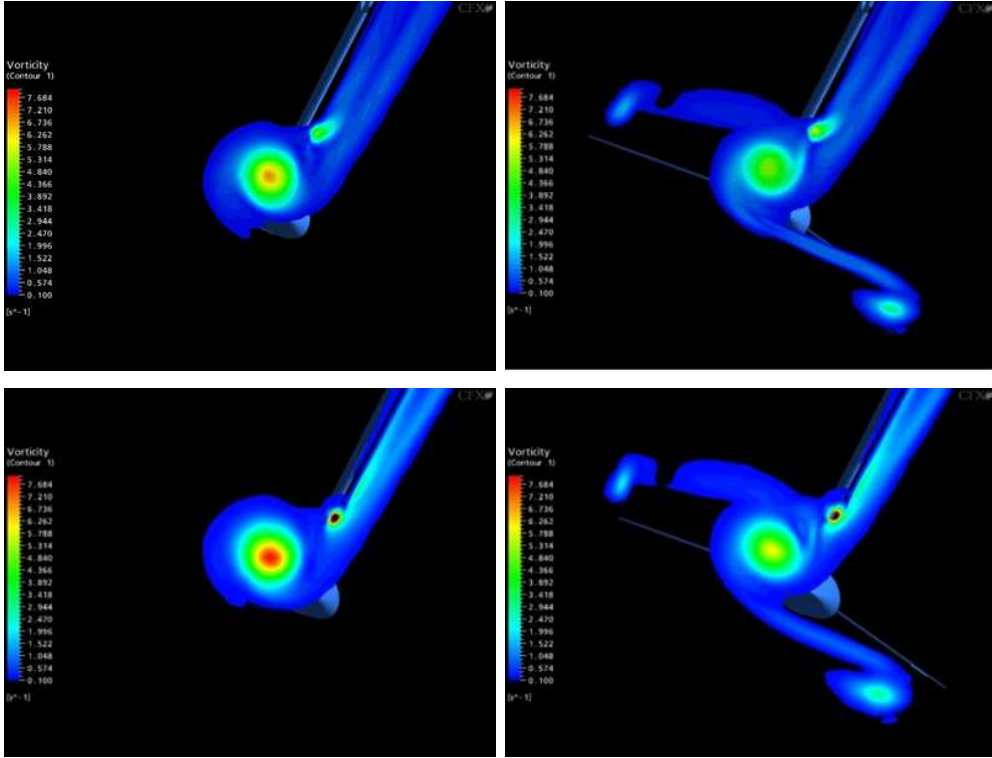


Figure 5: Cut plane of the vorticity field in the appendage wake. Top row: without (left) and with (right) winglets at 0 degree yaw angle. Bottom row: without (left) and with (right) winglets at 1.5 degree yaw angle.

with the latter having a strong impact on the vorticity evolution in the appendage wake. This effect is even stronger when increasing the yaw angle and therefore the lift induced recirculation (see Figure 5). Indeed, this vorticity reduction can be related to a reduction of the induced drag on keel and bulb, which is considered to be the most important beneficial effect induced by the presence of winglets.

The possibility to accurately predict the laminar-turbulent transition represents a big step forward in naval hydrodynamics, in particular for appendage design. Indeed, in this domain, the optimization process is often governed by trade-off analyses where pressure and viscous drag play one versus the other. A typical example is given by the comparison between a slender bulb and a shorter one (for constant ratio weight/volume). If the former usually guarantees a lower pressure drag, this advantage is counteracted by a larger viscous drag due to the larger wetted surface. For this comparison, an accurate estimation of the transition location is required to predict the viscous component of the drag with an acceptable precision. Indeed, bulb and keel are often designed to work in a transitional regime where slight difference in shape can induce a significant change on the location where laminar-turbulent transition occurs.

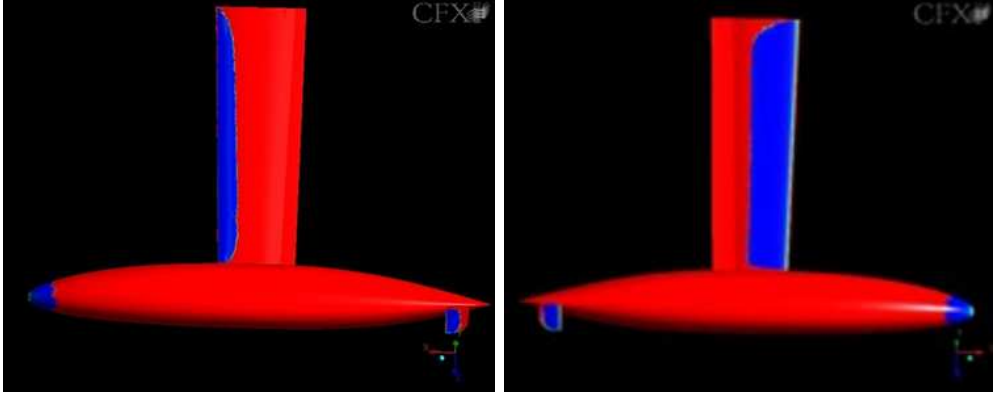


Figure 6: Results of the CFD transition analysis: transition location on suction side (left) and pressure side (right) of the appendages. Laminar regions are shown in red, turbulent ones in blue.

As illustrated in Section 2.2, the transition model adopted is able to take into account not only natural transition mechanisms but also transition due to free-stream turbulence. In order to calibrate the model on the configuration we were interested in, experimental measurements have been carried on in the NCR's $9m \times 9m$ wind tunnel in Ottawa (Canada). A 1.5:1 model scale (larger than the full scale!) of the appendages was necessary in order to match the actual Reynolds number. A large amount of experimental data have been generated for the CFD calibration, including global and local (on each appendage element) force components, transition locations on keel and bulb, sensitivity analysis with respect to freestream turbulence intensity.

An example of simulation detecting the laminar-turbulent transition on the appendage surface for an upwind configuration is displayed in Figure 6. A quantitative comparison versus experimental measurements of laminarity extension on the different appendage elements is given in Table 1. These results show the ability of the model in predicting with acceptable accuracy the transition location.

Component	Wind Tunnel	CFD
Bulb	7-15 %	8 %
Keel (Pressure side)	12-23%	24%
Keel (Suction side)	62 %	57%

Table 1: Comparison between experimental and numerical predictions for transition location.

5.2 Hull dynamics and free-surface

In the yacht design context, a numerical tool able to accurately predict forces and attitudes is of utmost importance since it may reduce the need of carrying out expensive experimental sessions in towing tank facilities. In this respect, the numerical scheme presented in Section 2.3 for the prediction of boat dynamics can be a powerful tool. Many potential applications are being explored and range from the dynamic response in waves to manoeuvring. We expect this kind of numerical investigation could become the standard in the coming years.

Thus far, in the context of the America's Cup design, this approach has been used to reproduce towing tank experiments [5, 13]. Two IACC hull shapes, that will be referred to as Hull 1 and Hull 2, have been considered. The two hulls have different bow designs and towing tank experiments have been carried out to estimate drag and sink at different boat speeds.

In Figure 7 we show the time history of the sink value starting from the initial sink position, correspondent to the hydrostatic equilibrium, and evolving through a damped oscillation towards the hydrodynamic equilibrium. The wave pattern around the two hulls at convergence are displayed in Figure 8.

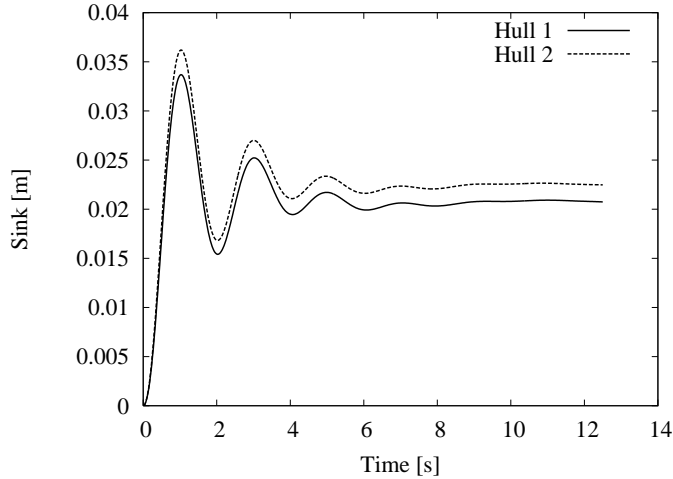


Figure 7: Time evolution of sink for the two hulls.

The numerical results show a good agreement in terms of forces and sink movement. A comparison between the total drag on Hull 1 obtained with the numerical simulations and the towing tank measurements at different boat speed is given in Figure 9, left. The error is consistently lower than 2% for all boat speeds. A similar comparison for the sink values at different boat speeds is presented in Figure 9, right. Again, we see a good correlation between numerical and experimental results.

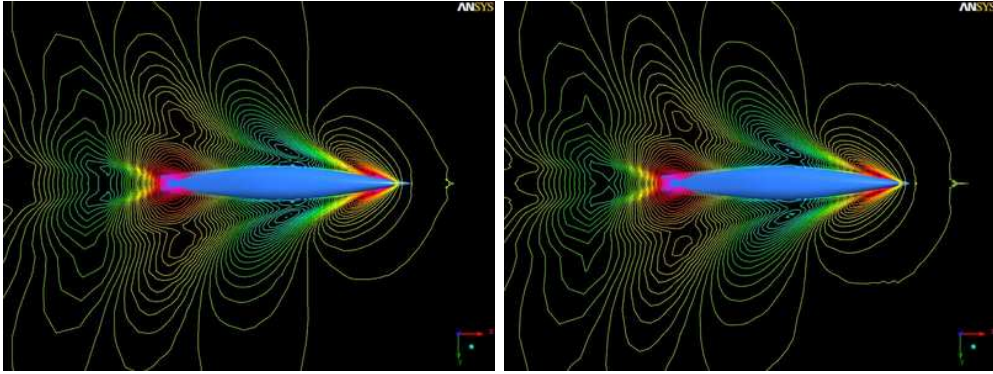


Figure 8: Wave patterns for Hull 1 (left) and Hull 2 (right) with a boat speed of 10 kts.

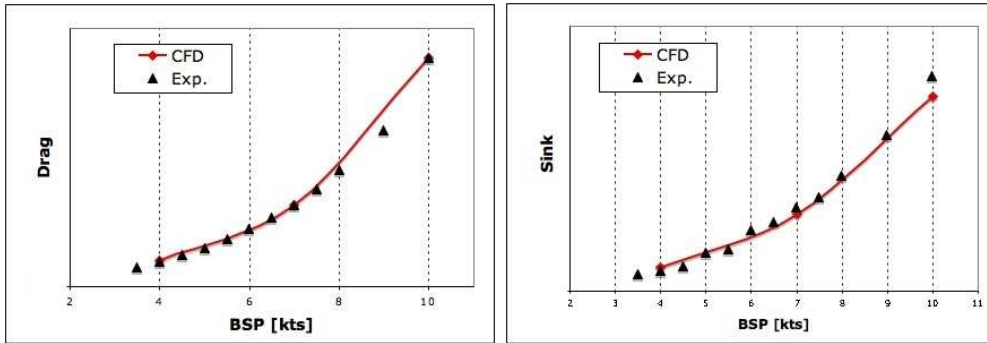


Figure 9: Comparison between towing tank measurements and numerical predictions for Hull 1: drag(left) and sink (right) *vs.* boat speed.

5.3 Sail trimming optimization

Finding the optimal trimming of all the cables and sheets governing the sails represents a challenging task and a very useful goal to speed up the the design process, and this is true because sails are always designed so that the best performances (in terms of driving force, for instance) can be reached within some given wind and trimming ranges. For this goal, an extensive campaign of simulations predicting the sails behavior before they are built can provide the designers a number of extremely useful hints for considerable enhancements, with evident benefits in terms of money and time saving. From the practical point of view, most part of the simulations have been carried on by changing the length of the main and the gennaker sheets, two cables which control the angle of attack of the two sails with respect to the incident wind direction. In Figure 10 we report a sequence of test cases where the air velocity vector field is plot on a 20 m height plane for three different gennaker configurations. From left to right, the gennaker sheet (GS) is

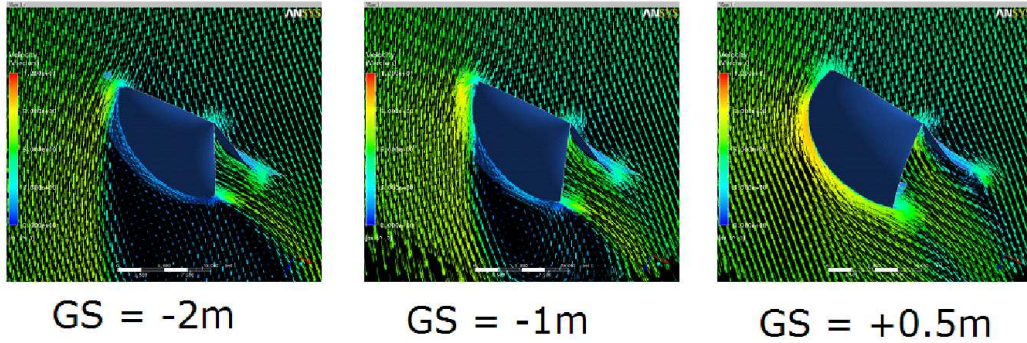


Figure 10: Final sail shapes for three different gennaker sheet (GS) trimmings (steady simulations)

eased out from $GS = -2.0\text{ m}$ to $GS = +0.5\text{ m}$ with respect to the design configuration which represents the reference for any adjustment and corresponds to $GS = 0.0\text{ m}$. It can be noticed that the most pulled-in case ($GS = -2.0\text{ m}$) shows a large separated region which extends from the leading to the trailing edge of the gennaker and this region reduces as the GS is eased out. The last case ($GS = +0.5\text{ m}$) shows an attached flow which follows the sail surfaces without any visible recirculation. In Figure 11 the driving force is plot as function of the gennaker sheet trimming, and the simulation confirms that the design setting ($GS = 0.0\text{ m}$) is the one which gives the larger driving force, so the best performance.

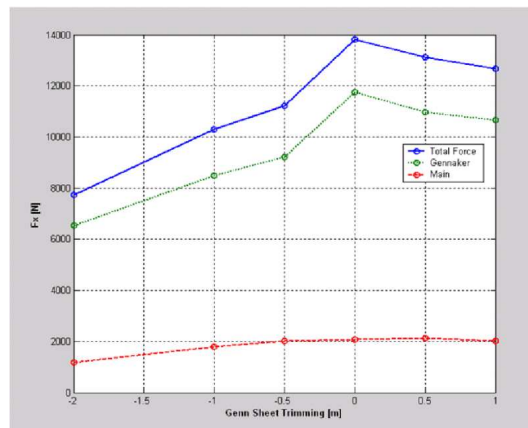


Figure 11: Driving force as function of the gennaker trimming (steady simulations)

5.4 Unsteady Sail Simulations

As introduced in section 3.5, unsteady simulations allow the investigation of the sail dynamics (the real evolution of the sail shape over time) and the stability properties of the structure. Moreover, the force history on sails, the frequencies of the structural vibrations and any periodic oscillation can also be easily monitored. For all these reasons, when the designers need a deeper investigation of the sail behavior, the unsteady approach can become extremely useful and an important source of information which can not be retrieved by simpler steady runs. In Figure 12 we compared the same sail simulation at different times, highlighting with a red solid line the left boundary of the big wake behind the gennaker. At $T = 6.5$ s it can be noticed that a small recirculation bubble appears close to the gennaker leading edge and the driving force on sails reaches its maximum value (see plot on the top-right corner). At $T = 18.5$ s the bubble has clearly enlarged, pushing away the left wake boundary so that the incident flow is now less deflected by the presence of the gennaker, this is clear by comparing the new wake boundary with the dashed line referring to the precedent case and kept on the second figure as reference. This reduced flow deflection leads to a smaller driving force acting on sails (because of the third Newton's law). Hence, unsteady simulations allow a truly physical resolution of the fluid flow over the time and highlight the effects of the dynamics of the turbulent wakes on many design parameters, like the evolution of the driving force or the sail stability properties under the action of unsteady loads.

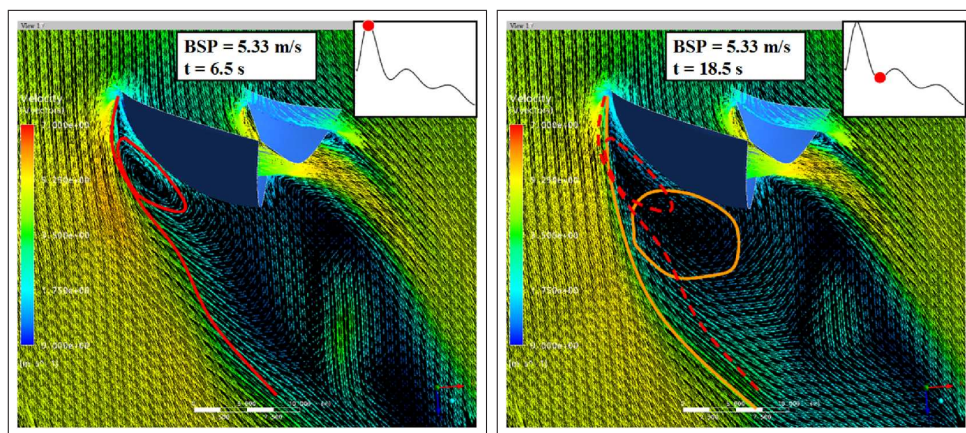


Figure 12: Fluid flow and driving force (in top-right corners) at two time instants, $T = 6.5$ s (left) and $T = 18.5$ s (right), for an unsteady fluid-structure simulation.

Conclusions

We have presented a review of the main results on numerical fluid-dynamic modelling obtained in the framework of the partnership between the Ecole Polytechnique Fédérale

de Lausanne and the Alinghi Team during the last two editions of the America's Cup.

We have highlighted the importance that CFD analysis is achieving in the design process of a racing yacht, devoting a particular attention to those modelling techniques that represent a step forward in this field.

Among them, we have presented and discussed through numerical examples the recent advances in turbulence and transition modelling, boat dynamics and wind-sail fluid-structure interaction.

References

- [1] R. Azcueta. *Computation of Turbulent Free-Surface Flows Around Ships and Floating Bodies*. Phd thesis, 2001.
- [2] R. Azcueta. RANSE Simulations for Sailing Yachts Including Dynamic Sinkage & Trim and Unsteady Motions in Waves. In *High Performance Yacht Design Conference*, pages 13–20, Auckland, 2002.
- [3] G. W. Cowles, N. Parolini, and M. L. Sawley. Numerical Simulation using RANS-based Tools for America's Cup design. In *Proceedings of the 16th Chesapeake Sailing Yacht Symposium*, Annapolis, USA, 2003.
- [4] C. W. Hirt and B. D. Nichols. Volume of Fluid (VOF) Method for the Dynamics of Free Boundaries. *J. Comp. Phys.*, 39:201–225, 1981.
- [5] M. Lombardi. Simulazione Numerica della Dinamica di uno Scafo. Master thesis, Politecnico di Milano, 2006.
- [6] R. E. Mayle. The Role of Laminar-Turbulent Transition in Gas Turbine Engines. *J. Turbomachinery*, 113:509–537, 1991.
- [7] R. E. Mayle and A. Schulz. The Path to Predicting Bypass Transition. *J. Turbomachinery*, 119:405–411, 1997.
- [8] F. R. Menter. Improved Two-Equation $k-\omega$ Turbulence Model for Aerodynamic Flows. Technical report, 1992. NASA TM-103975.
- [9] F. R. Menter. Two-Equation Eddy-Viscosity Turbulence Models for Engineering Applications. *AIAA Journal*, 32(8):1598–1605, 1994.
- [10] F. R. Menter, R. Langtry, S. Volker, and P. G. Huang. Transition Modelling for General Purpose CFD Codes. In *ERCRAFT Int. Symp. Engineering Turbulence Modelling and Measurements*, 2005.
- [11] Nicola Parolini and Alfio Quarteroni. Numerical simulation for yacht design. In *Proceedings of the 6th Hellenic-European conference on computer mathematics and its applications (HERCMA)*., 2004.

- [12] Nicola Parolini and Alfio Quarteroni. Mathematical models and numerical simulations for the America's Cup. *Computer Methods in Applied Mechanics and Engineering*, 194(9-11):1001–26, 2005.
- [13] Nicola Parolini and Alfio Quarteroni. Modelling and numerical simulation for yacht design. In *26th Symposium on Naval Hydrodynamics*, Arlington, 2007. Strategic Analysis Inc.
- [14] P. M. Richelsen. "Beregning af vindpvrirkede bdsejl". PhD thesis, Technical University of Denmark, 1987. in Danish.
- [15] G. E. Schneider and M. J. Raw. Control Volume Finite-Element Method for Heat Transfer and Fluidflow Using Colocated Variables. *Num. Heat Trans.*, 11:363–400, 1987.
- [16] K. Sieger, R. Schiele, F. Kaufmann, S. Wittig, and W. Rodi. A Two-Layer Turbulence Model for the Calculation of Transitional Boundary-Layers. *ERCRAFTAC bulletin*, 24:44–47, 1995.
- [17] A. M. O. Smith and N. Gamberoni. Transition, Pressure Gradient and Stability Theory. Technical report, 1956. Douglas Aircraft Company, Long Beach, Calif. Rep. ES 26388.
- [18] D. C. Wilcox. Reassessment of the Scale-Determining Equation for Advanced Turbulence Models. *AIAA Journal*, 26:1299–1310, 1988.

MOX Technical Reports, last issues

Dipartimento di Matematica “F. Brioschi”,
Politecnico di Milano, Via Bonardi 9 - 20133 Milano (Italy)

- 25/2008** D. DETOMI, N. PAROLINI, A. QUARTERONI:
Mathematics in the wind
- 24/2008** V. BACCHELLI, A. VENEZIANI, S. VESSELLA:
Corrosion detection in a 2D domain with a polygonal boundary
- 23/2008** S. HYSING, S TUREK, D. KUZMIN, N. PAROLINI, E. BURMAN, S. GANESAN, L. TOBISKA:
Quantitative benchmark computations of two-dimensional bubble dynamics
- 22/2008** F. NOBILE, R. TEMPONE:
Analysis and implementation issues for the numerical approximation of parabolic equations with random coefficients
- 21/2008** P. ANTONIETTI, E. SÜLI:
Domain Decomposition Preconditioning for Discontinuous Galerkin Approximations of Convection-Diffusion Problems
- 20/2008** F. DAVID, S. MICHELETTI, S. PEROTTO:
Model adaption enriched with an anisotropic mesh spacing for advection-diffusion-reaction systems
- 19/2008** S. BADIA, F. NOBILE, C. VERGARA:
Robin-Robin preconditioned Krylov methods for fluid-structure interaction problems
- 18/2008** L. BONAVENTURA, S. CASTRUCCIO, P. CRIPPA, G. LONATI:
Geostatistical estimate of PM10 concentrations in Northern Italy: validation of kriging reconstructions with classical and flexible variogram models
- 17/2008** A. ERN, S. PEROTTO, A. VENEZIANI:
Hierarchical model reduction for advection-diffusion-reaction problems
- 16/2008** L. FORMAGGIA, E. MIGLIO, A. MOLA, A. SCOTTI:
Numerical simulation of the dynamics of boat by a variational inequality approach